Wave-vector power spectrum of the local tunneling density of states: Ripples in a *d*-wave sea

L. Capriotti*
Kavli Institute of Theoretical Physics, University of California, Santa Barbara, California 93106-4030, USA

D. J. Scalapino† and R. D. Sedgewick‡
Department of Physics, University of California, Santa Barbara, California 93106-9530, USA

(Received 26 February 2003; published 29 July 2003)

A weak scattering potential imposed on a CuO_2 layer of a cuprate superconductor modulates the local density of states $N(x,\omega)$. In recently reported experimental studies, scanning-tunneling maps of $N(x,\omega)$ have been Fourier transformed to obtain a wave-vector power spectrum. Here, for the case of a weak scattering potential, we discuss the structure of this power spectrum and its relationship to the quasiparticle spectrum and the structure factor of the scattering potential. Examples of quasiparticle interferences in normal metals and *s*- and *d*-wave superconductors are discussed.

DOI: 10.1103/PhysRevB.68.014508 PACS number(s): 74.25.Jb, 74.50.+r

I. INTRODUCTION

A weak scattering potential imposed on the CuO_2 layer of a cuprate superconductor creates ripples in the local tunneling density of states $N(x,\omega)$ due to quasiparticle interference scattering. It was suggested that scanning-tunneling measurements of the spatial and frequency structure of $N(x,\omega)$ could provide information on the k and ω dependence of the gap.[1] Recently, the introduction of high-resolution Fourier-transform scanning-tunneling microscopy[2–4] (FT-STM) has provided a powerful new technique for studying this. In this approach, a BISCO crystal is cleaved exposing a BiO_2 layer. Then an STM measurement of the local tunneling conductance $dI(V,x)/dV$ is taken over a predetermined $L\times L$ grid of points that cover a region of order 600 Å$\times$600 Å. Assuming that the tunneling conductance is proportional to the underlying density of states of the CuO_2 layer,[5] these measurements give an STM map of the local tunneling density of states $N(x,\omega)$ with $\omega=eV$. This map is then Fourier transformed,

$$N(q,\omega)=\sum_{x_l\in(L\times L)} e^{-iq\cdot x_l}N(x_l,\omega), \tag{1}$$

and the wave-vector power spectrum

$$P(q,\omega)=\frac{|N(q,\omega)|^2}{L^2} \tag{2}$$

determined. Typically, the square root of the power spectrum, which is proportional to the magnitude of $N(q,\omega)$, is plotted and we will follow that practice as well. Here, we will discuss the structure of $P(q,\omega)$ and its relationship to the quasiparticle spectrum and the structure factor of the scattering potential.

For an isotropic *s*-wave superconductor with a circular normal-state Fermi surface, the ripples in $N(x,\omega)$ produced by a weak scattering center form a circular pattern whose amplitude and wavelength depend upon the bias voltage $\omega=eV$. However, if the gap has $d_{x^2-y^2}$ symmetry, the ripples emanating from a scattering center appear as a characteristic set of rays whose wavelength and amplitude vary with their angular direction and the size of the bias voltage $\omega=eV$.[1,6] Two examples of this are shown in Fig. 1. It is the STM measurements of these modulations in $N(x,\omega)$ that provide

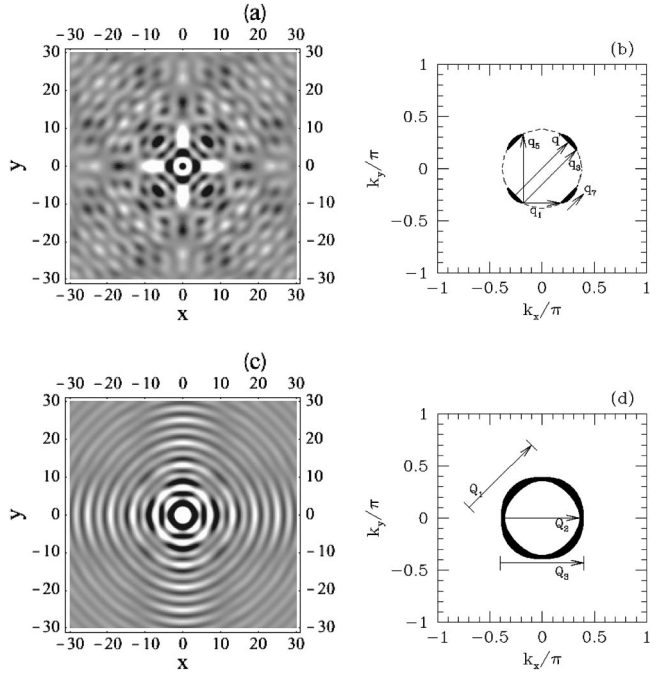

FIG. 1. (a) The local tunneling density of states $N(x,\omega)$ due to scattering from a weak potential at the origin (Ref. 1), for (a) $\omega=0.5\Delta_0$ and (c) $\omega=1.1\Delta_0$. The length scale is set by k_F^{-1}. These results were obtained for a cylindrical Fermi surface with a *d*-wave gap $\Delta(\theta)=\Delta_0\cos(2\theta)$. The contours of the solid regions in (b) and (d) correspond to the points where $\omega=\sqrt{\epsilon_k^2+\Delta^2(\theta)}$ for $\omega=0.5\Delta_0$ and $1.1\Delta_0$, respectively. The dashed line in (b) is the Fermi surface for the noninteracting system. The $\mathbf{q}_\alpha(\omega)$ wave vectors in (b), introduced in Ref. 4, connect the tips of various contours and $\mathbf{q}'(\omega)$ connects what would be a diagonal nesting vector for the normal state Fermi surface. The $\mathbf{Q}_\alpha(\omega)$ wave vectors shown in (d) are the relevant nesting vectors when $\omega>\Delta_0$.

information on the wave-vector and frequency dependence of the gap. Indeed, in their FT-STM power spectrum study of BISCO, Hoffman *et al.*[2] and McElroy *et al.*[4] found frequency-dependent structure in $P(q,\omega)$ which they argued was consistent with the Fermi surface dependence of $\Delta(k)$ as seen from angle-resolved photoemission spectroscopy (ARPES) measurements.[7] In this work,[2,4] these authors suggested that the FT-STM data could be analyzed in terms of a set of frequency-dependent wave vectors $\mathbf{q}_\alpha(\omega)$ which connect the tips of the constant energy contours specified by the quasiparticle dispersion relation

$$\omega = \sqrt{\epsilon_k^2 + \Delta_k^2}. \tag{3}$$

The contours of the solid regions shown in Figs. 1(b) and 1(d) are the constant quasiparticle energy contours for a cylindrical Fermi surface $\epsilon_k = k^2/2m - \mu$ with a gap $\Delta_k = \Delta_0 \cos 2\theta$ for $\omega = 0.5\Delta_0$ and $1.1\Delta_0$, respectively. Also shown in Fig. 1(b) are several of the $\mathbf{q}_\alpha(\omega)$ wave vectors introduced in Ref. 4. The wave vector $\mathbf{q}'(\omega)$ is an additional wave vector that we will discuss. The wave vectors $\mathbf{q}_1(\omega)$ and $\mathbf{q}_5(\omega)$, along with their symmetry-related counterparts (not shown), are associated with the structure of the ripples in $N(x,\omega)$ seen along the x and y axes of Fig. 1(a). Likewise, the wave vectors $\mathbf{q}_3(\omega)$, $\mathbf{q}'(\omega)$, and $\mathbf{q}_7(\omega)$ determine the structure of the ripples along the 45° axes of Fig. 1(a).In conjunction with this experimental work, Wang and Lee[8] recently reported numerical calculations for the case of a single impurity which clearly showed the quasiparticle interference arising from $\mathbf{q}_1(\omega)$ and $\mathbf{q}_7(\omega)$. In addition, as ω is varied these calculations showed that a rich, kaleidescopelike structure appears in the wave-vector power spectrum when it is folded back into the first Brillouin zone.

In a similar way, for $\omega = 1.1\Delta_0$, the wave vectors Q_α shown in Fig. 1(d) determine the structure of $N(x,\omega)$ seen in Fig. 1(c). Here the ripples along the x and y axes are associated with Q_2 and Q_3 (and their symmetry-related counterparts in the y direction), while those along the diagonal are associated with Q_1 (and its counterparts). In practice, when $\omega \sim \Delta_0$, inelastic scattering leads to a damping of the ripples in $N(x,\omega)$, making the structure in $|N(x,\omega)|$ associated with the Q_α wave vectors difficult to detect.

Now, the quasiparticle interference pattern shown in Figs. 1(a) and 1(c) are for a single impurity. For a particular surface region over which the STM measurements are made, there will be an array of scatterers leading to a complex overlap of ripples. Here we will discuss how the Fourier-transformed wave-vector power spectrum $P(q,\omega)$ allows one to disentangle the quasiparticle interference effects from the static structure factors of the scatterers. In Sec. II we show that for the case of a weak scattering potential, $P(q,\omega)$ factors into one piece which contains information on the nesting properties of the Fermi surface times a piece which is proportional to the static structure factor of the scatterers. We also note that these measurements contain information on the one-electron self-energy. Various examples are analyzed to show the type of information that is in principle contained in the FT-STM data. In Sec. III, the case of a layered two-dimensional (2D) superconductor is studied with results for both s-wave and d-wave gaps discussed. Section IV contains our conclusions, and Appendixes A and B contain more details of the calculations.

II. FT-STM POWER SPECTRUM OF A 2D NORMAL METALLIC LAYER

To begin, we first consider the case of a normal metallic 2D layer. Suppose it is exposed to a weak potential

$$V = \sum_s \int d^2x\, \delta\epsilon(x)\, \psi_s^\dagger(x)\, \psi_s(x), \tag{4}$$

with $\delta\epsilon(x)$ an energy shift at x. For a BISCO-like system this local energy change $\delta\epsilon(x)$ could arise from secondary effects associated with disorder away from the CuO_2 plane, the regular potential of the BiO_2 layer, or possibly a weak static stripe potential. This interaction creates a ripple in the one-electron Green's function, leading to a modulation in the local tunneling density of states. For the case of a weak potential which we will focus on, a Born approximation is appropriate so that the single-particle Green's function is given by

$$G(x,x',\omega) = G_0(x-x',\omega) + \int d^2x''\, G_0(x-x'',\omega) \times \delta\epsilon(x'')\, G_0(x''-x',\omega). \tag{5}$$

Here, $G_0(x,\omega)$ is the Green's function of the unperturbed system. Then the change in the single-spin tunneling density of states at position x is given by

$$\delta N(x,\omega) = -\frac{1}{\pi}\,\mathrm{Im} \int d^2x''\, G_0(x-x'',\omega)\, \delta\epsilon(x'') \times G_0(x''-x,\omega). \tag{6}$$

Taking the spatial Fourier transform of $\delta N(x,\omega)$, on the $L \times L$ grid of points $\{\mathbf{x}_l\}$ specified by the STM measurements, one finds, for $q \neq 0$, that

$$N(q,\omega) = \sum_{x_l \in (L\times L)} e^{-iq\cdot x_l}\, \delta N(x_l,\omega) = -\frac{\delta\epsilon(q)}{\pi}\,\mathrm{Im}\,\Lambda(q,\omega), \tag{7}$$

with

$$\Lambda(q,\omega) = \int d^2x e^{iq\cdot x} G_0(x,\omega) G_0(-x,\omega) \tag{8}$$

and

$$\delta\epsilon(q) = \int \frac{d^2x}{a^2}\, \delta\epsilon(x) e^{-iq\cdot x}. \tag{9}$$

Here a is the lattice spacing of the $L\times L$ STM grid and $q = 2\pi(n_x, n_y)/La$ with n_x and n_y integers running from $-L/2+1$ to $L/2$. The wave-vector power spectrum of the local tunneling density of states, Eq. (2), is therefore given by

$$P(q,\omega)=\frac{1}{N}\left|\frac{1}{\pi}\mathrm{Im}\,\Lambda(q,\omega)\right|^2|\delta\epsilon(q)|^2. \tag{10}$$

Here $N=L\times L$ is the number of sites in the sampled region. Thus, in the weak scattering Born approximation $P(q,\omega)$ separates into a piece $|\mathrm{Im}\,\Lambda(q,\omega)/\pi|^2$ which describes the quasiparticle interference and a piece $|\delta\epsilon(q)|^2$ which is the static structure factor $S(q)$ of the scattering potential.

For the random impurity case, one could imagine making STM maps over a large number of different $L\times L$ regions. Then by averaging the structure factor over these maps one would obtain

$$\frac{\langle|\delta\epsilon(q)|^2\rangle}{N}=n_i\delta\epsilon^2 \quad (q\neq 0), \tag{11}$$

where n_i is the area impurity concentration and $\delta\epsilon$ is a site energy shift. In this case, $P(q,\omega)$ would simply be proportional to $n_i\delta\epsilon^2$ times the quasiparticle interference factor from a single impurity. However, this is not the way the experiments are done. Rather, a single STM map on a finite $L\times L$ grid of points covering a specific region is measured. In this case, $|\delta\epsilon(q)|^2$ versus q exhibits fluctuations blurring the image of $|\mathrm{Im}\,\Lambda(q,\omega)/\pi|$, although one can still resolve structure in false color 2D (q_x,q_y) maps of $|N(q,\omega)|$. However, as discussed in Appendix A, by averaging the power spectrum over blocks of width $(\Delta q_x,\Delta q_y)$ about each q, the fluctuations can be reduced if the impurities are randomly distributed. Naturally, this reduces the momentum resolution. However, if the change in q of the quasiparticle interference response is predominately along a given momentum direction, one can average over a region of q values perpendicular to the direction of interest, reducing the fluctuations but maintaining the q resolution in the direction of interest. Here we will assume that a suitable average has been done and use the impurity structure factor given by Eq. (11). Appendix A contains a further discussion of the effect of impurity induced fluctuations.

For the case in which the scattering occurs from a regular lattice such as the Bi lattice, one has

$$|\delta\epsilon(q)|^2=\delta\epsilon^2N^2\delta_{q,G_n}. \tag{12}$$

Here $\mathbf{G}_n$ is a reciprocal lattice vector of the Bi lattice along with the satellite wave vectors associated with the supermodulation of the BiO_2 layer. One could also have a ''random'' array of stripe domains with

$$\langle|\delta\epsilon(q)|^2\rangle\simeq N_i\left\{\frac{\Gamma/\pi}{(q_x-Q_x)^2+\Gamma^2}+\frac{\Gamma/\pi}{(q_y-Q_y)^2+\Gamma^2}+(q_x\rightarrow -q_x,q_y\rightarrow -q_y)\right\}\delta\epsilon^2. \tag{13}$$

Here $Q_x=2\pi/l_x$ with l_x the stripe spacing, $2\pi/\Gamma$ is the characteristic size of a domain, and N_i is the average number of domains in an $L\times L$ region. Here we have taken only the first Q_x harmonic. The form factor associated with the charge distribution of the stripes suppresses the response at higher multiples of Q_x. We will examine the effect of an array of scattering centers in Sec. III.

Turning next to the quasiparticle interference response, we begin by looking at $G_0(x,\omega)$ for a free 2D electron gas. In this case, for $\omega>0$,

$$G_0(x,\omega)=\int\frac{d^2k}{(2\pi)^2}\frac{e^{ik\cdot x}}{\omega-\epsilon_k+i\delta}=-i\pi N(0)H_0^{(1)}(k(\omega)r), \tag{14}$$

with $\epsilon_k=k^2/2m-\mu$ and $\mu=k_F^2/2m$. Here $N(0)=m/2\pi$ is the single-spin electron density of states for the 2D free electron gas, $H_0^{(1)}$ is the zeroth-order Hankel function of the first kind, $r=|x|$, and

$$k(\omega)=k_F\sqrt{1+\frac{\omega}{\mu}}. \tag{15}$$

When $k(\omega)r$ is large,

$$G_0(x,\omega)\sim -iN(0)\left(\frac{2\pi}{k(\omega)r}\right)^{1/2}e^{i[k(\omega)r-(\pi/4)]} \tag{16}$$

and the spatial modulation of $\delta N(x,\omega)$ which varies as the square of $G_0(x,\omega)$ is characterized by a wave vector

$$q(\omega)=2k_F\sqrt{1+\frac{\omega}{\mu}}. \tag{17}$$

The quasiparticle interference response function $\Lambda(q,\omega)$ for the 2D electron gas is calculated in Appendix B. The result of this calculation shows[9] that

$$\frac{1}{\pi}\mathrm{Im}\,\Lambda(q,\omega)=\begin{cases}\dfrac{8\pi N^2(0)}{q\sqrt{q^2-4k^2(\omega)}} & \text{for } q>2k(\omega),\\ 0 & \text{for } q<2k(\omega).\end{cases} \tag{18}$$

Thus, the wave-vector power spectrum for the 2D free electron gas has a cusp at q equals $2k(\omega)$. Here $\mathrm{Im}\,\Lambda(q,\omega)$ vanishes for $q<2k(\omega)$ and diverges as $[q-2k(\omega)]^{-1/2}$ as q approaches $2k(\omega)$ from larger values. As noted in Appendix A, $\mathrm{Re}\,\Lambda(q,\omega)$ has a similar cusp as q approaches $2k(\omega)$ from below. Basically, there is just a shift of phase of $\pi/2$ in $\Lambda(q,\omega)$ when q passes trough $2k(\omega)$. If the impurities are dilute, but the scattering from a given impurity is strong, one still has $P(q,\omega)$ proportional to the impurity concentration. However, in this case,[10] because of the phase of the t-matrix one will have singularities on both sides of $2k(\omega)$.

The experimental FT-STM data have been reported as the square root of the power spectrum or the ''magnitude'' $|N(q,\omega)|$ of the Fourier transform of the STM measurement of the local conductance map. Here we will follow this convention. For the case of weak Born scattering, the magnitude of $N(q,\omega)$ is proportional to $|\mathrm{Im}\,\Lambda(q,\omega)/\pi|$. For the 2D electron gas, in Fig. 2, we have plotted $|N(q,\omega)|$ normalized

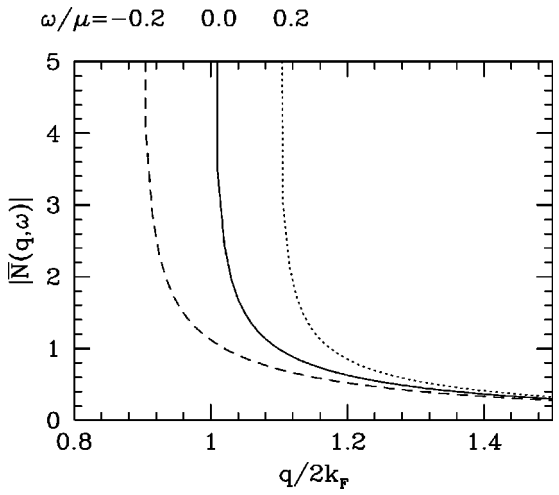

FIG. 2. Plot of the normalized $|N(q,\omega)|$ vs q for a free electron gas for various values of ω/μ.

to $\sqrt{n_i}N(0)|\delta\epsilon|/\mu$ versus q for various values of ω/μ. Here, with q in units of $2k_F$ one has

$$|\bar{N}(q,\omega)| = \frac{|N(q,\omega)|}{\sqrt{n_i}N(0)\left(\frac{|\delta\epsilon|}{\mu}\right)} = \frac{1}{2q}\frac{1}{\sqrt{q^2-\left(1+\frac{\omega}{\mu}\right)}} \tag{19}$$

for $(1+\omega/\mu)<q/2k_F$. As shown in Fig. 2, for the weak scattering case $|\bar{N}(q,\omega)|$ has a one-sided square root singularity at $q/2k_F=(1+\omega/\mu)^{1/2}$. This singularity is cut off and the response peak varies as $(\ell k_F)^{1/2}$ when the quasiparticle mean free path is taken into account. In this case

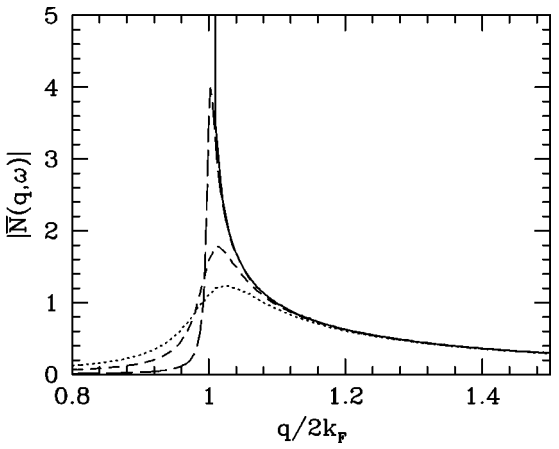

FIG. 3. Plot of the normalized mean free path corrected $|N(q,\omega)|$ vs q for an electron gas with $\omega=0$. Here $\Gamma=(\ell k_F)^{-1}$: $\Gamma=0$ (solid line), $\Gamma=0.01$ (long-dashed line), $\Gamma=0.05$ (dashed line), and $\Gamma=0.1$ (dotted line).

$$|\bar{N}(q,\omega)| = \frac{1}{2\pi q}\int_{-1}^{q^2-1} d\epsilon \frac{\Gamma}{\left(\frac{\omega}{\mu}-\epsilon\right)^2+\Gamma^2}\frac{1}{\sqrt{q^2-(1+\epsilon)}}, \tag{20}$$

with $\Gamma=(\ell k_F)^{-1}$. Plots of $|\bar{N}(q,\omega)|$ versus q for $\omega=0$ and several different values of Γ are shown in Fig. 3.

Similarly, for an anisotropic system with

$$\epsilon_k = \frac{k_x^2}{2m_x}+\frac{k_y^2}{2m_y}-\mu, \tag{21}$$

one finds that

$$\frac{1}{\pi}\mathrm{Im}\,\Lambda(q_x,q_y,\omega) = \begin{cases} \dfrac{2}{\pi\gamma}m_x^2 \dfrac{1}{\sqrt{q_x^2+\gamma^2q_y^2}} \dfrac{1}{\sqrt{q_x^2+\gamma^2q_y^2-8m_x(\omega+\mu)}} & \text{for } q_x^2+\gamma^2q_y^2>8m_x(\mu+\omega), \\ 0 & \text{for } q_x^2+\gamma^2q_y^2<8m_x(\mu+\omega), \end{cases} \tag{22}$$

with $\gamma^2=m_x/m_y$. In this case the cusp in the power spectrum follows a locus determined by

$$q_x^2+\gamma^2q_y^2=8m_x(\mu+\omega), \tag{23}$$

which reflects the elliptical Fermi surface. In Fig. 4, we have plotted $|N(q,\omega)|$ for $\omega=0$ and $\gamma=3$ normalized to $\sqrt{n_i}(m_x/2\pi)|\delta\epsilon|/\mu$, which gives

$$|\bar{N}(q_x,q_y,\omega)| = \frac{1}{2\gamma}\frac{1}{\sqrt{q_x^2+\gamma^2q_y^2}}\frac{1}{\sqrt{q_x^2+\gamma^2q_y^2-\left(1+\frac{\omega}{\mu}\right)}}, \tag{24}$$

with q_x and q_y measured in units of $2k_F^x=2(2m_x\mu)^{1/2}$. Here, we see that $|\bar{N}(q,0)|$ vanishes inside the ellipse, Eq. (23), and has a square root divergence as q approaches the ellipse. There is a reduction $\gamma=(m_y/m_x)^{1/2}$ in the strength of the cusp along the q_y direction relative to the q_x direction that reflects the fact that the joint density of states which enters $\Lambda(q,\omega)$ depends on the curvature of the Fermi surface.

Turning now to the case of a tight-binding band, we consider first the simple nearest-neighbor hopping band for a square lattice with unit lattice spacing:

$$\epsilon_k = -2t(\cos k_x+\cos k_y)-\mu. \tag{25}$$

The Fermi surface is shown in Fig. 5 for $\mu=-t$, corresponding to a small filling $\langle n\rangle\approx 0.31$, which we have chosen

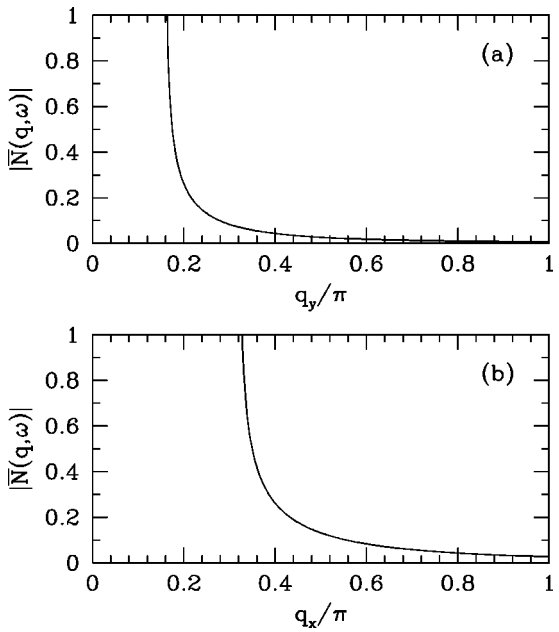

FIG. 4. Plot of the normalized $|N(q,\omega)|$ vs q, Eq. (24), for an elliptical Fermi surface with $\gamma^2=m_x/m_y=9$ and $\omega=0$. In (a) $q_x=0$ and in (b) $q_y=0$.

to illustrate what happens when $\mathrm{Im}\,\Lambda(q,w)$ is folded back into the first Brillouin zone. In the following tight-binding band structure calculations, we will assume that $N(x,\omega)$ is measured on a grid of points corresponding to the sites of the lattice. In this case,

$$\Lambda(q,\omega)=\frac{1}{N}\sum_k G_0(k+q,\omega)G_0(k,\omega), \tag{26}$$

with

$$G_0(k)=\frac{1}{\omega-\epsilon_k+i\delta\,\mathrm{sgn}(\omega)}. \tag{27}$$

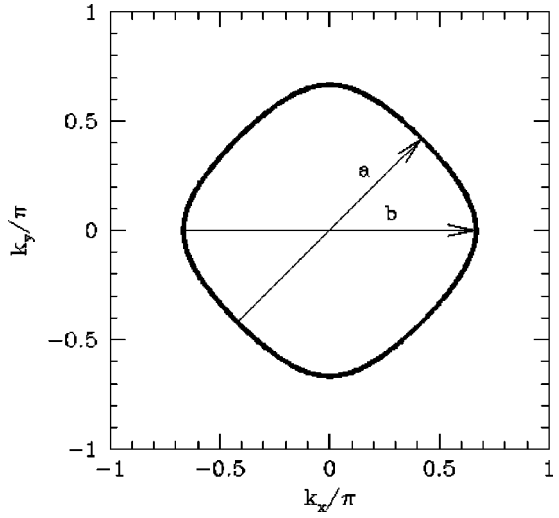

FIG. 5. Fermi surface of a near-neighbor tight-binding band, Eq. (28), with $\mu/t=-1.0$ corresponding to a site filling $\langle n\rangle\approx 0.31$.

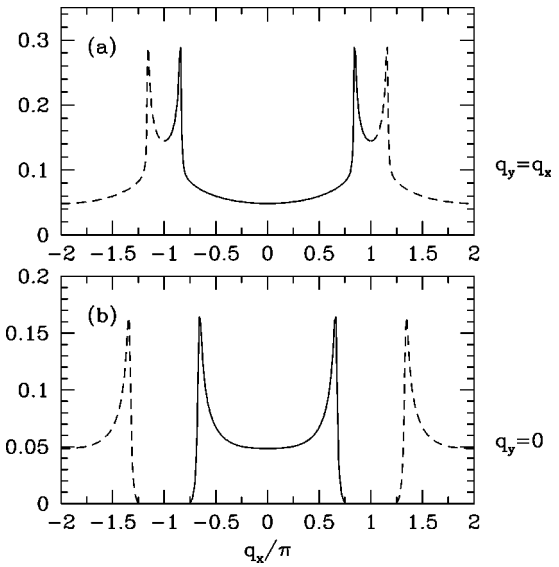

FIG. 6. $|\mathrm{Im}\,\Lambda(q,\omega)/\pi|$ for the tight-binding band, Eq. (25), with $t=1$ vs q for $\omega=0$ and (a) the diagonal cut a and (b) the horizontal cut b indicated in Fig. 5. The dashed curves show the results in the second Brillouin zone. For cut a, $2k_F^{xy}\simeq 0.8\pi$, so the solid curve in the first Brillouin looks similar to the free electron response. However, for cut b, $2k_F^{x}\simeq 1.3\pi$, so that the dashed curve in (b) looks similar to the free electron response and the solid curve in the first Brillouin zone results from folding the dashed curve back into the first zone.

Here, $N=L\times L$ is the number of lattice sites and k and q are defined in the first Brillouin zone with components running from $-\pi$ to π. We have set the lattice spacing $a=1$. This choice of the grid simplifies the calculations but has the consequence that all results are folded back into the first Brillouin zone. It is this downfolding that leads to the kaleidoscopic patterns in the numerical results shown in Ref. 8. In the experimental FT-STM measurements,[2,4] a smaller grid spacing was used leading to a q-space power spectrum which looks more like the extended zone picture for the q vectors of interest.

Carrying out the momentum sum in Eq. (26), we find the results for $|\mathrm{Im}\,\Lambda(q,\omega)/\pi|$ shown in Fig. 6. Here, in Fig. 6(a), q varies along the diagonal a cut shown in Fig. 5 with $q_x=q_y$. In this case, $|\bar{N}(q,\omega)|$ exhibits a similar cusp to that of the free electron system when $|q_x|\geqslant 2k_F^{xy}=2\cos^{-1}[-(\mu+\omega)/4t]$. This same type of behavior is shown as the dashed curve for the b cut with $q_y=0$ in Fig. 6(b), where we have displaced the numerical results by $\pm 2\pi$ corresponding to an extended zone scheme. Here, the cusp occurs for $|q_x|\geqslant 2k_F^{x}=2\cos^{-1}[-(2t+\mu+\omega)/2t]$ which is greater than π for the b cut of Fig. 5. In practice, the numerical data are obtained in the ''reduced'' $(-\pi,\pi)$ zone so that the $q_y=0$ b cut appears as the solid curve shown in Fig. 6(b). As ω is increased, the characteristic q values can move across the boundary of the first zone and be mapped back via a reciprocal lattice vector. This can then lead to a situation in which the square root singularity is approached from smaller q values with $|\bar{N}(q,\omega)|$ vanishing when q exceeds a critical value as shown by the solid curve in Fig. 6(b). As noted, it is this

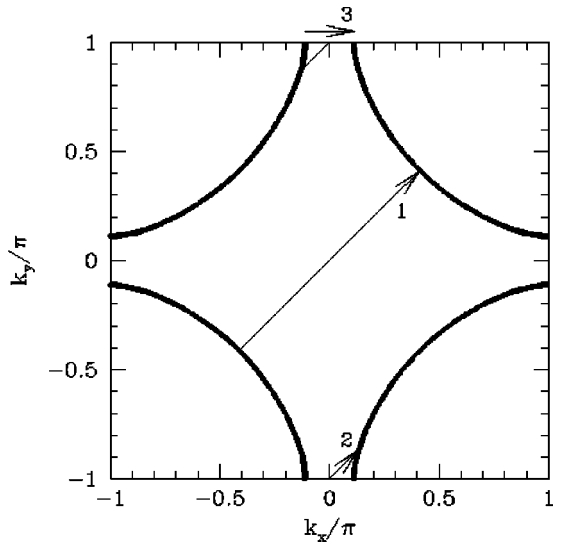

FIG. 7. Fermi surface of a tight-binding band with near and next-near hopping, Eq. (28), with $t'/t=-0.3$ and $\mu/t=-1.0$.

folding of the FT-STM power spectrum into the reduced zone that leads to the kaleidoscopic 2D (q_x,q_y) patterns for different ω values which have been reported.[8]

Finally, consider the case of a tight-binding band, like that found for BISCO. Here, one has a next-near-neighbor hopping t' so that

$$\epsilon_k=-2t(\cos k_x+\cos k_y)-4t'\cos k_x\cos k_y-\mu. \quad (28)$$

The Fermi surface for $t'/t=-0.3$ and $\mu/t=-1.0$ is shown in Fig. 7. Results of a numerical calculation for $\mathrm{Im}\,\Lambda(q,\omega)/\pi$ for this case are plotted in Figs. 8(a) and 8(b) for $q_y=0$ and $q_x=q_y$, respectively. For $q_y=0$, the nesting vector 3 is shown in Fig. 7. If we consider the closed Fermi surface around (π,π), one can see that the two points of this closed Fermi surface that are connected by the wave vector

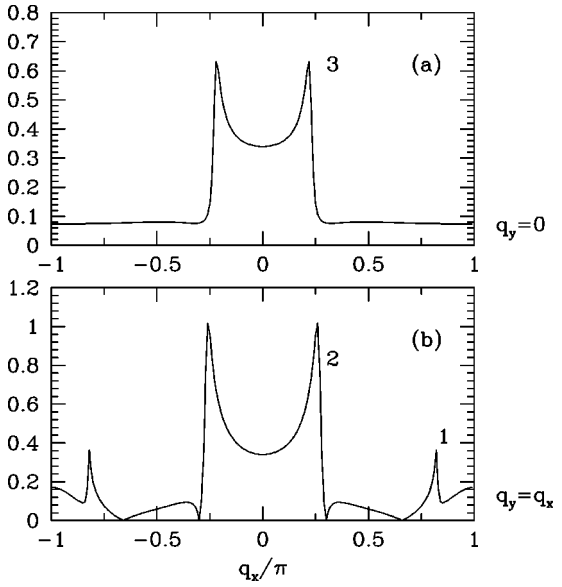

FIG. 8. $|\mathrm{Im}\,\Lambda(q,\omega)/\pi|$ vs q for $\omega=0$ for the tight-binding Fermi surface shown in Fig. 7. (a) $q_y=0$ and (b) $q_x=q_y$.

labeled 3 have Δq greater than π. In fact, $\Delta q/\pi\simeq 1.76$, so that when this is folded back into the first Brillouin zone, the cusp occurs at $\Delta q/\pi\simeq -0.24$. Also, as we saw previously in Fig. 6(a) the cusp rises from smaller values of q in the reduced zone although in an extended zone scheme it would be approached from larger q values just as in the free electron case. The peaks in the response for $q_x=q_y$ shown in Fig. 8(b) arise from the nesting vectors labeled 1 and 2 in Fig. 7.

To conclude this section on the normal state, we consider an electron-phonon system with a self-energy $\Sigma(\omega)$ which depends only upon the frequency. In this case, the momentum that enters the Hankel function giving $G(x,\omega)$ is

$$k(\omega)\cong k_F+\frac{(\omega-\Sigma(\omega)}{v_F}. \quad (29)$$

The real part of the self-energy leads to a shift in the wavelength of the modulations and the imaginary part of Σ leads to their exponential decay on a scale $\ell=v_F/[-2\Sigma_2(\omega)]$. This behavior is reflected in a shift in the position and a rounding of the cusp in the power spectrum $P(q,\omega)$. For values of ω which are small compared to a typical phonon frequency

$$k(\omega)\simeq k_F+\frac{(1+\lambda)\omega}{v_F}, \quad (30)$$

with $\lambda=2N(0)|g|^2/\Omega_0$ the dimensionless electron-phonon interaction strength. Here g is the effective electron-phonon coupling and Ω_0 a typical phonon energy. As ω increases $2k_F(\omega)$ will reflect the detailed dependence of both the real and imaginary parts of $\Sigma(\omega)$.

III. FT-STM POWER SPECTRUM OF A SUPERCONDUCTOR

Next consider the case of a superconductor. Here, for an on-site energy perturbation, we have[1]

$$\delta N(x,\omega)=-\frac{1}{\pi}\mathrm{Im}\int d^2x'[G(x-x',\omega)G(x'-x,\omega) -F(x-x',\omega)F(x'-x,\omega)]\delta\epsilon(x'), \quad (31)$$

with $G(x,\omega)$ the usual single-particle propagator,

$$G(x,\omega)=\int \frac{d^2k}{(2\pi)^2}e^{ik\cdot x}\frac{\omega+\epsilon_k}{\omega^2-\epsilon_k^2-\Delta_k^2+i\delta}, \quad (32)$$

and $F(x,\omega)$ the anomalous Gor'kov propagator,

$$F(x,\omega)=\int \frac{d^2k}{(2\pi)^2}e^{ik\cdot x}\frac{\Delta_k}{\omega^2-\epsilon_k^2-\Delta_k^2+i\delta}. \quad (33)$$

In this case[11]

$$\Lambda(q,\omega)=\int \frac{d^2k}{(2\pi)^2}[G(k+q,\omega)G(k,\omega) -F(k+q,\omega)F(k,\omega)]. \quad (34)$$

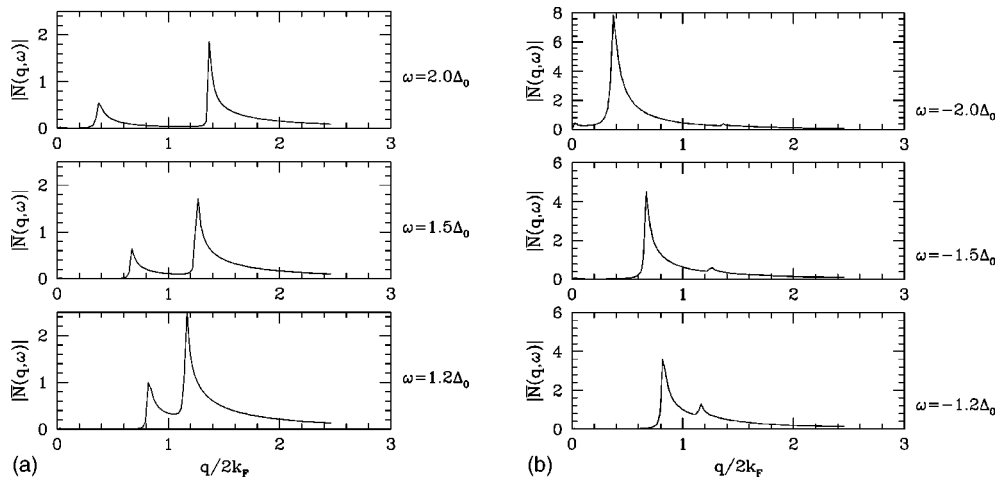

FIG. 9. Plot of the normalized $|N(q,\omega)|$ vs q for an s-wave superconductor with a cylindrical Fermi surface and $\Delta/\mu=0.1$. (a) Results for positive values of $\omega=eV$ and (b) for negative values of ω.

For a 2D s-wave superconductor with $\Delta_k=\Delta$ and $\epsilon_k=k^2/2m-\mu$, these Green's functions have characteristic wave vectors

$$k_{\pm}(\omega)=k_F\left[1\pm\frac{\sqrt{\omega^2-\Delta^2}}{\mu}\right]^{1/2}. \tag{35}$$

The wavelength of the ripples in $\delta N(x,\omega)$ is set by $2k_{\pm}(\omega)$. For $\omega<\Delta$, the ripples exponentially decay. If the impurity perturbation involved a change in the size of the gap, there would be a quasiparticle interference contribution involving $k_+(\omega)-k_-(\omega)=2k_F\sqrt{\omega^2-\Delta^2}/\mu$. The ripples associated with this contribution vary on a length scale set by v_F/Δ which is of order the coherence length rather than k_F^{-1}. It is this type of spatial oscillation that is responsible for the Tomasch oscillations.[12] While Tomasch ripples at $Q_T(\omega)=k_+(\omega)-k_-(\omega)$ are not present for the case of a charge impurity in an isotropic s-wave superconductor, they can appear for a d-wave superconductor as discussed below.

As shown in Appendix B, it is straightforward to evaluate $\mathrm{Im}\,\Lambda(q,\omega)$ for an s-wave BCS superconductor and one finds that

$$\frac{1}{\pi}\mathrm{Im}\,\Lambda(q,\omega)=4\pi N^2(0)\left(\frac{\omega-\sqrt{\omega^2-\Delta^2}}{\sqrt{\omega^2-\Delta^2}}\right)\frac{1}{q}\,\frac{1}{\sqrt{q^2-4k_-^2(\omega)}} \tag{36}$$

for $2k_-(\omega)<q<2k_+(\omega)$ and

$$\frac{1}{\pi}\mathrm{Im}\,\Lambda(q,\omega)$$
$$=4\pi N^2(0)\left(\frac{\omega-\sqrt{\omega^2-\Delta^2}}{\sqrt{\omega^2-\Delta^2}}\right)\frac{1}{q}\,\frac{1}{\sqrt{q^2-4k_-^2(\omega)}}$$
$$+4\pi N^2(0)\left(\frac{\omega+\sqrt{\omega^2-\Delta^2}}{\sqrt{\omega^2-\Delta^2}}\right)\frac{1}{q}\,\frac{1}{\sqrt{q^2-4k_+^2(\omega)}} \tag{37}$$

for $2k_+(\omega)<q$. More generally, for an electron-phonon system the frequency-dependent complex gap $\Delta(\omega)$ would replace Δ. Normalizing by $\sqrt{n_i}N(0)|\delta\epsilon|/\mu$, as previously done for the free electron case, we have plotted $|\bar{N}(q,\omega)|$ versus q in Fig. 9 for a BCS s-wave superconductor with $\Delta/\mu=0.1$. The coherence factors in Eq. (36) and (37) give more weight to the $2k_+(\omega)$ cusp for positive values of ω associated with a bias voltage that probes the empty states, Fig. 9(a), while the $q=2k_-(\omega)$ cusp is enhanced when the bias is reversed as shown in Fig. 9(b).

We turn next to the case of a d-wave superconductor with

$$\Delta_k=\Delta_0(\cos k_x-\cos k_y)/2 \tag{38}$$

and a band structure given by Eq. (28) with $t'/t=-0.3$ and $\mu=-1.0$. The Fermi surface for these parameters is shown as a dashed line in Fig. 10(a). The contours of the solid regions correspond to the loci of points where $\omega=\sqrt{\epsilon_k^2+\Delta_k^2}$ for $\omega=0.5\Delta_0$ in Fig. 10(a) and $\omega=1.1\Delta_0$ in Fig. 10(b). Results for $|\mathrm{Im}\,\Lambda(q,\omega)/\pi|$ at various values of ω less than Δ_0 are shown in Fig. 11(a) for $q_x=q_y$ and Fig. 11(b) for $q_y=0$. For the diagonal cut with $q_x=q_y$, there is a response at the wave vector $\mathbf{q}_7(\omega)$ shown in Fig. 10(a) which connects the end points of the $\omega^2=\epsilon_k^2+\Delta_k^2$ contour. This peak is similar to the peak we have seen in the case of the ellipse discussed in the previous section. There are two identical contributions coming from the two contours on opposite sides of the Fermi surface. As the bias voltage $eV=\omega$ increases, one sees that $q_7(\omega)$ peak moves to larger values of momentum. This reflects the increase in magnitude of the wave vector $q_7(\omega)$ as ω is increased and can provide information on the k dependence of the Fermi surface and gap.[2,4] In addition, there is a contribution coming from $\mathbf{q}_3(\omega)$ which connects the tips of two opposite contours which increases more slowly with ω. Finally, there is a response associated with $\mathbf{q}'$ shown in Fig. 10(a). This is the response due to the wave vector labeled 1 in Fig. 7 and shown in the diagonal $q_x=q_y$ response of the normal metal with this same band structure in Fig. 8(b). Approximate analytic results for the d-wave case are given in Appendix B, Eqs. (B14) and (B17).

Similarly in Fig. 11(b), for $q_y=0$ one finds structure associated with the wave vectors $\mathbf{q}_1$ and $\mathbf{q}_5$ shown in Fig.

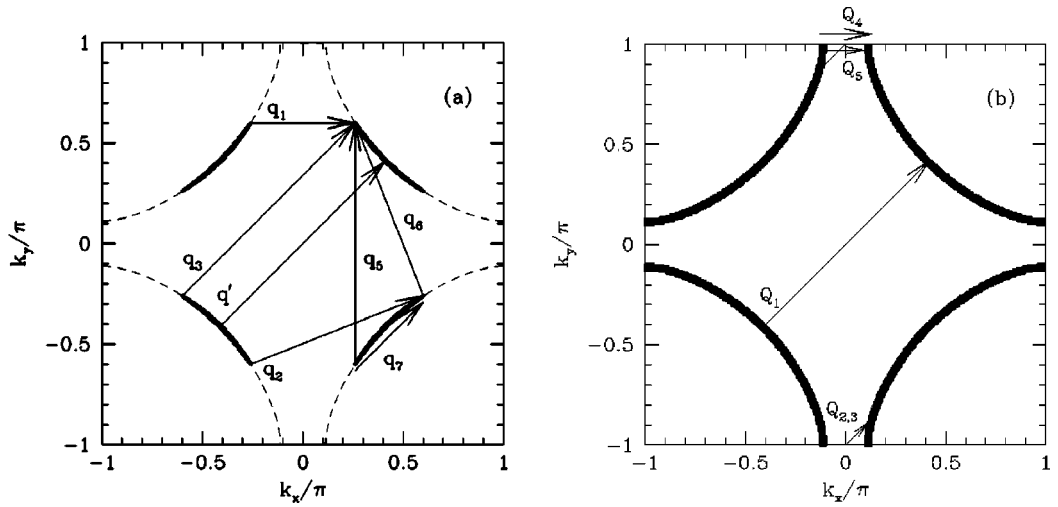

FIG. 10. Characteristic wave vectors for a *d*-wave superconductor with a tight-binding band, Eq. (28), with $t'/t=-0.3$, $\mu/t=-1.0$, and $\Delta_0=0.1t$. The contours of the solid regions correspond to the points where $\omega=\sqrt{\epsilon_k^2+\Delta_k^2}$ with (a) $\omega=0.5\Delta_0$ and (b) $\omega=1.1\Delta_0$. The dashed line in (a) shows the Fermi surface of the noninteracting system. In (b) Q_3 and Q_5 (Q_4 and Q_2) connect the innermost (outermost) surfaces while Q_1 connects the outermost surfaces.

10(a). As discussed by McElroy *et al.*,[4] this structure arises from a peak in the joint density of states associated with the overlap of the ends of two opposite $\omega^2=\epsilon_k^2+\Delta_k^2$ contours. Just as for the case of the elliptical Fermi surface previously discussed, the strength of the cusp depends upon the curvature of the dispersion. The increase of $q_1(\omega)$ with increasing ω again provides information on the Fermi surface and Δ_k. The peak at $q_5(\omega)$ initially increases with ω and would continue to increase in an extended zone but here, for $\omega\sim0.25$, it is reflected back into the first Brillouin zone. Finally, there is a weak cusp at low momentum $q_t(\omega)$ associated with the Tomasch interference process.

Note that the response seen in $|\overline{N}(q,\omega)|$ associated with quasiparticle interference is actually characterized by a continuous curving cusp in the (q_x,q_y) plane whose intensity is related to the joint density of the k and $k+q$ quasiparticle states. When we take into account all four quadrants, the structure in the power spectrum $P(q,\omega)$ in the first Brillouin zone becomes much richer. Not only are there cusps associated with scattering processes confined to similar contour regions in quadrants 2 and 4, which give rise to a cusp whose major axis is perpendicular to that due to quadrants 1 and 3, there are cusps from scattering processes between the four nodal regions. In addition, there is the response associated with the nodal wave vector $\mathbf{q}'$. In order to see this more clearly, we have calculated $\Lambda(q,\omega)$ for the case in which $t'=0$. In Fig. 12 we compare the results for $|\mathrm{Im}\,\Lambda(q,\omega)/\pi|$ calculated with $t'=0$ [Fig. 12(a)] and with $t'/t=-0.3$ [Fig. 12(b)]. In both cases, we clearly see the contributions of $\mathbf{q}_3$ and $\mathbf{q}_7$. In addition, a $\mathbf{q}'$ contribution from the nodal region is also visible. The $\mathbf{q}_3$ contribution is weaker for the case in which $t'=0$. In this case we also find that $|\mathbf{q}_3|<|\mathbf{q}'|$ as one can see from the insets in the figures.

When ω is greater than Δ_0, structure in $|N(q,\omega)|$ is associated with the Q_α vectors shown in Fig. 10(b), for $\omega=1.1\Delta_0$. In this case, for $q_x=q_y$, $|N(q,\omega)|$ exhibits structure at $q_x=Q_1$, Q_2, and Q_3; see Fig. 13(a). The weak structure at large momentum transfer Q_1 is similar to the structure for the normal state labeled "1" in Fig. 8, since the gap vanishes along the diagonal. The structures at Q_2 and Q_3

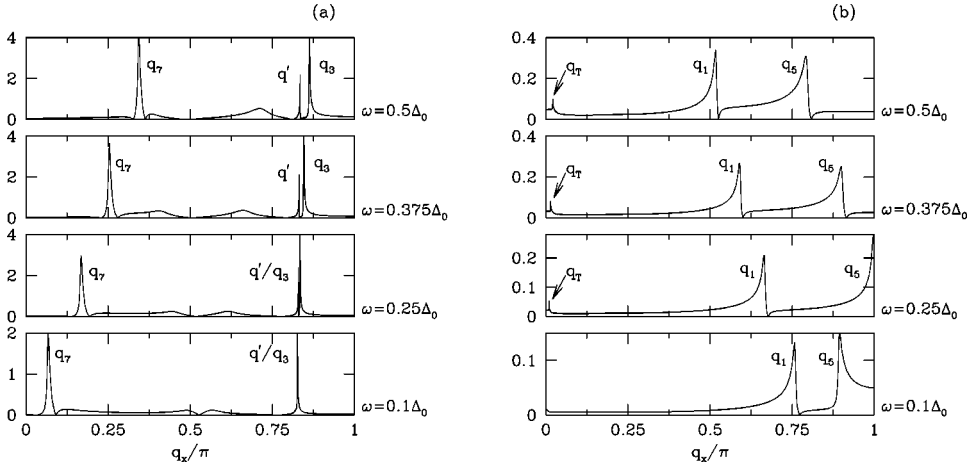

FIG. 11. $|\mathrm{Im}\,\Lambda(q,\omega)/\pi|$ vs q for a *d*-wave superconductor with a tight-binding band given by Eq. (28) with $t'/t=-0.3$, $\mu/t=-1.0$, and $\Delta_0=0.1t$. Here (a) shows results for a diagonal cut for $q_x=q_y$ and (b) shows results for a horizontal $q_y=0$ cut. The q_α and q' vectors are shown in Fig. 10(a).

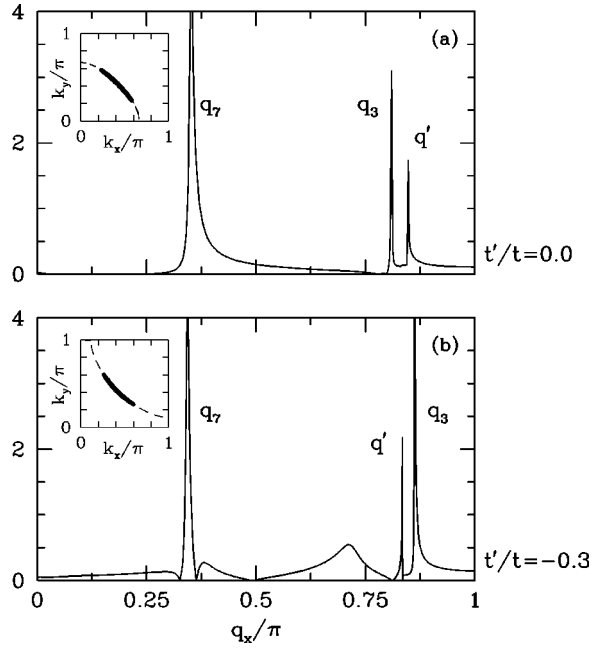

FIG. 12. $|\mathrm{Im}\,\Lambda(q,\omega)/\pi|$ vs q for a diagonal cut in which $q_x = q_y$. (a) shows results for a tight-binding band with $t'/t=0$ and (b) shows results for $t'/t=-0.3$. $\omega=0.5\Delta_0$ and the other parameters are the same of Fig. 11.

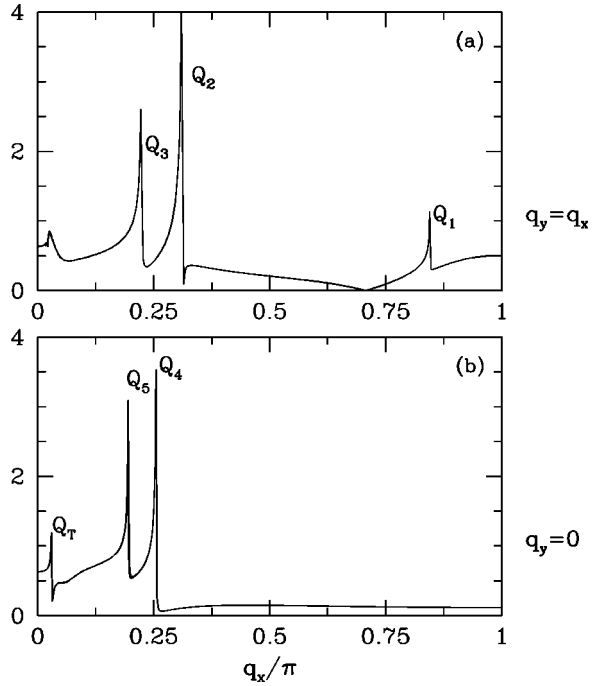

FIG. 13. $|\mathrm{Im}\,\Lambda(q,\omega)/\pi|$ vs q for a d-wave superconductor with a tight-binding band given by Eq. (28) with $t'/t=-0.3$, $\mu/t=-1.0$, $\Delta_0=0.1t$, and $\omega=1.1\Delta_0$. Here (a) shows results for a diagonal 45° cut for $q_x=q_y$ and (b) shows results for a horizontal $q_y=0$ cut. The Q_α vectors are shown in Fig. 10(b).

correspond to interference processes between the particlelike and holelike BCS quasiparticles. Just as for the s-wave case, for $\omega>0$, the coherence factor gives more weight to the Q_2 process. Results for $|N(q,\omega)|$ versus q_x for $q_y=0$ are shown in Fig. 13(b). In this case, structure appears associated with $q_x=Q_4$ and Q_5 with the coherence factors leading to a large response at Q_4 for positive ω. As noted earlier, in the cuprate superconductors lifetime effects suppress this $\omega>\Delta_0$ structure, making it difficult to see in the experimental studies.

The structure in the quasiparticle interference response can also be seen in the intensity map plots of $|\mathrm{Im}\,\Lambda(q,\omega)/\pi|$ over the (q_x,q_y) plane. One such map for $\omega=0.5\Delta_0$ is shown in Fig. 14. Here one sees that the response is characterized by continuous curving intensity cusps in the (q_x,q_y) plane. Like the case of the elliptical Fermi surface, the intensity can have significant variations along the cusps due to the curvature of the quasiparticles dispersion relation. Going out from the origin along $q_x=q_y$ as in Fig. 12(b), one first sees a bright (high-intensity region) cusp associated with q_7. At large momentum values along this same 45° line one sees a narrow bright line associated with q' scattering processes which connect the outer edges of the $\omega=\sqrt{\epsilon_k^2+\Delta_k^2}$ envelopes. Finally, the brighter, curved region of intensity near the (π,π) corner arises from q_3 interference processes associated with the inner boundaries of these contours. The bright regions near $(q_x/\pi=0.85,\ q_y/\pi=0.3)$ and $(q_x/\pi=0.3,\ q_y/\pi=0.85)$ arise from interference effects associated with q_2 and q_6 of Fig. 10(a).

Finally, we consider the response of a d-wave superconductor when there is an ordered stripe array of weak scattering centers. In Fig. 15 we show the ripples produced in $N(x,\omega)$ when the scattering centers form a stripelike structure oriented along the y axis with a spacing of four lattice sites. For the parameters we have chosen, $q_5(\omega)\simeq\pi/2$ for $\omega=0.5\Delta_0$ with Δ_0 the maximum value of the d-wave gap. As seen in Fig. 15, the ordered array of stripe scattering centers produces an oriented set of ripples. These give rise to the structure in $|N(q,\omega)|$ shown in Fig. 16 for $q\simeq\pi/2$. Here we have assumed that there is quasiparticle scattering from a

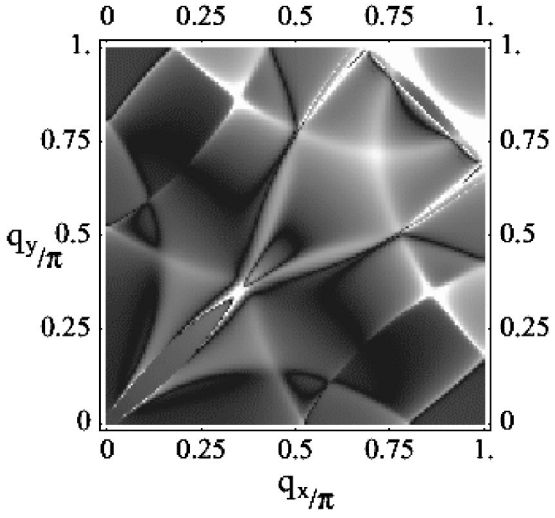

FIG. 14. Intensity map of the quasiparticle interference response $|\mathrm{Im}\,\Lambda(q,\omega)/\pi|$ for a d-wave superconductor plotted over the first (q_x,q_y) quadrant. Here, the band structure is given by Eq. (28) with $t'/t=0.3$ and $\mu=-1.0$; Δ_k is given by Eq. (38) and the bias is $\omega=0.5\Delta_0$.

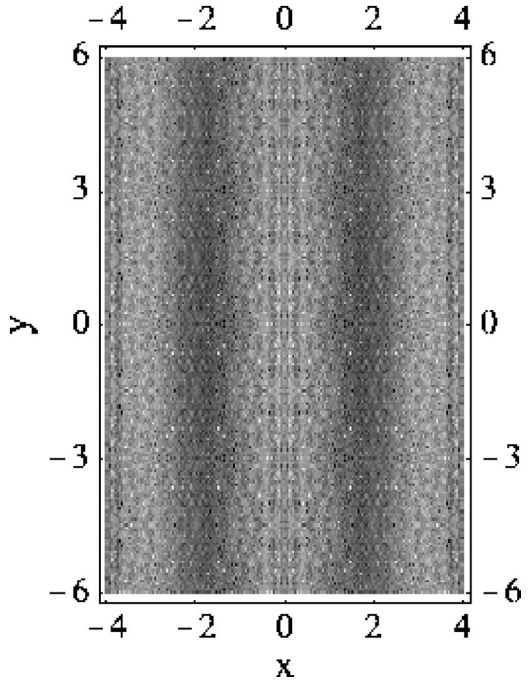

FIG. 15. Ripples in $N(x,\omega)$ when there is an ordered array of scattering centers running along the y axis. Here the spacing between the stripes corresponds to four lattice sites and $\omega=0.5\Delta_0$.

random array of impurities as well as the stripes. These contributions add incoherently so that

$$\langle|\delta\epsilon(q)|^2\rangle\sim\left[1+A\frac{\Gamma/\pi}{(q_x-Q_x)^2+\Gamma^2}\right]. \tag{39}$$

Here $Q_x=\pi/2$ and we have taken $\Gamma=0.01$ and $A=0.5$ in Fig. 16 to illustrate the possible interplay of the scattering from the random impurities and the stripes. The quasiparticle interference peak associated with q_1 moves to lower values

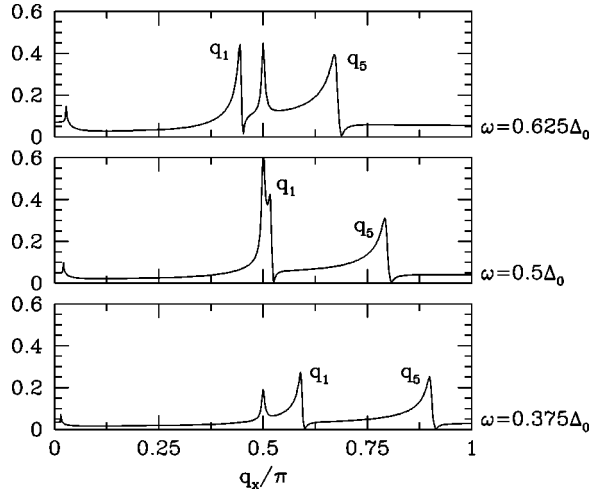

FIG. 16. Structure in $|\overline{N}(q,\omega)|$ vs q_x for random impurities and an ordered array of stripes separated by four lattice spacings. The quasiparticle interference peaks associated with $q_1(\omega)$ and $q_5(\omega)$, previously shown in Fig. 11(b), are seen along with a peak at $q\simeq0.5\pi$ which arises from the striped array of scattering centers.

of q_x as ω increases while the response associated with the ordered array of scattering centers remains fixed at $q_x\simeq0.5\pi$ and only its amplitude changes with ω. For larger values of A, the stripes would be the dominant feature while for smaller values of A scattering from the random impurities would dominate the power spectrum.

IV. CONCLUSIONS

Here we have discussed some detailed examples which illustrate what can be learned from FT-STM studies of layered materials. For the case of a weak potential perturbation we have seen that the wave-vector power spectrum of the local tunneling density of states, $P(q,\omega)$, contains information on the quasiparticle spectrum and the structure factor of the scatterers. This is also the case for dilute impurities even if they act as strong scattering centers and $\delta\epsilon$ is replaced by a t matrix. For a normal metal, one can determine information about the nesting properties of the Fermi surface from the loci of the **q**-space cusps for $\omega\rightarrow0$. In addition, the dressed Fermi velocity can be obtained from the ω dependence of the position of the cusp. In fact, from the ω dependence of the cusp position and its rounding, one can, in principle, obtain information on the real and imaginary parts of the electron self-energy.

In the superconducting state, one can also obtain information on both the wave-vector and frequency dependence of the gap $\Delta(k,\omega)$. Again, just as in the case of a normal metal, the signature of these quasiparticle interference effects are continuous ''arcs'' of cusps in **q** space. However, the intensity variation along the arcs may be large due to changes in the effective density of states associated with a given momentum transfer **q**, making the intensity appear more like spots. The rapid change in intensity is due to the small parameter Δ_0/t.

In addition to these effects, one can also obtain information on the static structure factor of the scattering potential $\langle|\delta\epsilon_q|^2\rangle$. As discussed in Appendix A, for the case of a local potential, averaging over a Δq_x by Δq_y block of q values about a given q leads to $\langle|\delta\epsilon_q|^2\rangle/N\simeq n_i\delta\epsilon^2$. However, if the scattering potential has long-range order, such as is the case for the BiO_2 over layer in the BISCO studies, one should see a q-dependent response in the wave-vector power spectrum of the local tunneling density of states for **q** values equal to the reciprocal lattice vectors of the BiO_2 layer. This response will be particularly strong for $\omega\simeq\Delta_0$. Similarly, it should be possible to see evidence of pinned stripes in the structure factor if they are present.[3]

As discussed in the Introduction, we have focused on the case of weak scattering. As noted, in this limit, where the Born approximation is adequate, one has a simple separation of the response into the quasiparticle interference effects which are contained in $\Lambda(q,\omega)$ and the structure factor of the scatterers which is contained in $\langle|\delta\epsilon_q|^2\rangle$. Of course, many-body interactions will give rise to additional effects. There will be screening, changing $\delta\epsilon_q$ to $\delta\epsilon_q/\epsilon(q,0)$ where $\epsilon(q,0)$ is the zero-frequency dielectric constant.[9] Furthermore, there will be vertex corrections so that, for example, for a strongly interacting normal system one will have

$$\Lambda(q,\omega)=\int \frac{d^2k}{(2\pi)^2}\Gamma(k,q,\omega)G(k+q,\omega)G(k,\omega), \tag{40}$$

with $\Gamma(k,q,\omega)$ the elastic vertex for momentum transfer q and zero energy transfer for an incoming particle with momentum k and energy ω. Similar vertex corrections will occur in the superconducting state. In addition, the quasiparticle dispersion relation can be altered by an interaction which breaks the translational symmetry,[13] leading to a different ω dependence of $|N(q,\omega)|$.

Finally, there is the form factor of the tunneling probe. Here we have neglected the momentum dependence of the tunneling matrix element and simply assumed that the conductance map was proportional to the local tunneling density of states $N(x,\omega)$. However, if this is not the case, a tunneling matrix element form factor

$$T(k)=\sum_l e^{ik\cdot l}T(l) \tag{41}$$

will enter so that for a superconductor

$$\Lambda(q,\omega)=\frac{1}{N}\sum_k T^*(k+q)T(k)[G(k+q,\omega)G(k,\omega) - F(k+q,\omega)F(k,\omega)]. \tag{42}$$

For example, a tunneling form factor

$$T(k)=(\cos k_x-\cos k_y) \tag{43}$$

has been suggested for the case of an STM tip on a cuprate superconductor.[5] However, because the average tunneling density of states in these STM experiments appears to vary linearly with V at low voltages, we have modeled the tunneling as a direct process and neglected its momentum dependence.

Note added in proof. For the case of strong scattering one can use a t-matrix to describe the single impurity problem. This can lead to resonant scattering processes and local structure in $N(x,\omega)$,[15] as well as alter the coherence factors[8,16] affecting $N(q,\omega)$. For the case of many impurities, one may well need to also take into account interference processes involving multiple impurity centers.[17]

ACKNOWLEDGMENTS

We would like to acknowledge useful discussions of the experimental FT-STM measurements with J.C. Davis, J.E. Hoffman, A. Kapitulnik, and K. McElroy. We also thank M.E. Flatté for discussions which rekindled our interest in this problem and S.A. Kivelson, P. Hirschfeld, R.L. Sugar, and L. Zhu for many helpful and insightful discussions during the course of our work. This work was supported by the National Science Foundation under Grant No. DMR02-11166. We would also like to acknowledge support provided by the Yzurdiaga gift to UCSB.

APPENDIX A: RANDOM IMPURITY STRUCTURE FACTOR

Suppose we have an $L\times L$ section of a lattice with a concentration of n_i impurities per unit area. Assume that if there is an impurity at site l it has a potential $\delta\epsilon(l)=1$, while if there is no impurity at site l, $\delta\epsilon(l)=0$. For a given random configuration of N_i impurities on $L\times L=N$ sites, corresponding to an area impurity concentration $n_i=N_i/N$, we have

$$\delta\epsilon(q)=\sum_l e^{iq\cdot l}\delta\epsilon(l). \tag{A1}$$

For this configuration of impurities we can define a power spectrum with

$$P(q)=\frac{|\delta\epsilon(q)|^2}{N}. \tag{A2}$$

There is of course a peak for $q=0$, where

$$P(0)=\frac{N_i^2}{N}. \tag{A3}$$

However, for other values of q, $P(q)$ fluctuates about n_i. If one were to average $P(q)$ over many realizations of independent impurity configurations,[14]

$$\langle P(q)\rangle=n_i \quad \text{for} \quad q\neq 0. \tag{A4}$$

However, if we have an $L\times L$ lattice with a fixed configuration of impurities, the power spectrum $P(q)$, given by Eq. (A2), will exhibit fluctuations. If we average $P(q)$ over blocks of q of width $(\Delta q_x,\Delta q_y)$ about each q, we can reduce these fluctuations. Naturally, at the same time, the momentum resolution will be reduced. Define a block-smoothed $P(q)$ average as follows:

$$\overline{P}(q)=\frac{1}{N(\Delta q_x,\Delta q_y)}{\sum_{\Delta q_x,\Delta q_y}}' P(q); \tag{A5}$$

here the prime on the sum indicates that $P(0)$ is replaced with n_i so that the $q=0$ peak is not broadened from the smoothing operation. The sum in Eq. (A5) is over a set of q points $(-\Delta q_x/2,\Delta q_x/2)$ and $(-\Delta q_y/2,\Delta q_y/2)$ about each q. Here $N(\Delta q_x,\Delta q_y)$ is the number of sites in the Δq_x by Δq_y block. We expect that the rms fluctuations of $\overline{P}(q)$ will decrease inversely as the square root of the number of q values in the Δq_x by Δq_y block.

For example, consider a lattice with $L=500$ and one configuration of random impurities with $n_i=0.01$. The power spectrum $P(q)$, given by Eq. (A2), versus q_x for $q_y=0$ is shown in Fig. 17(a). Figures 17(b) and 17(c) show similar plots for the smoothed power spectrum $\overline{P}(q)$, given by Eq. (A5), for square blocks with $\Delta q_x=\Delta q_y=2\pi(2d+1)/L$ for $d=5$ and $d=10$, respectively. Figure 17(d) shows $\overline{P}(q)$ for the case in which only $\Delta q_y=2\pi(2d+1)/L$ is averaged with $d=10$. The solid line in each of these figures is $n_i=0.01$.

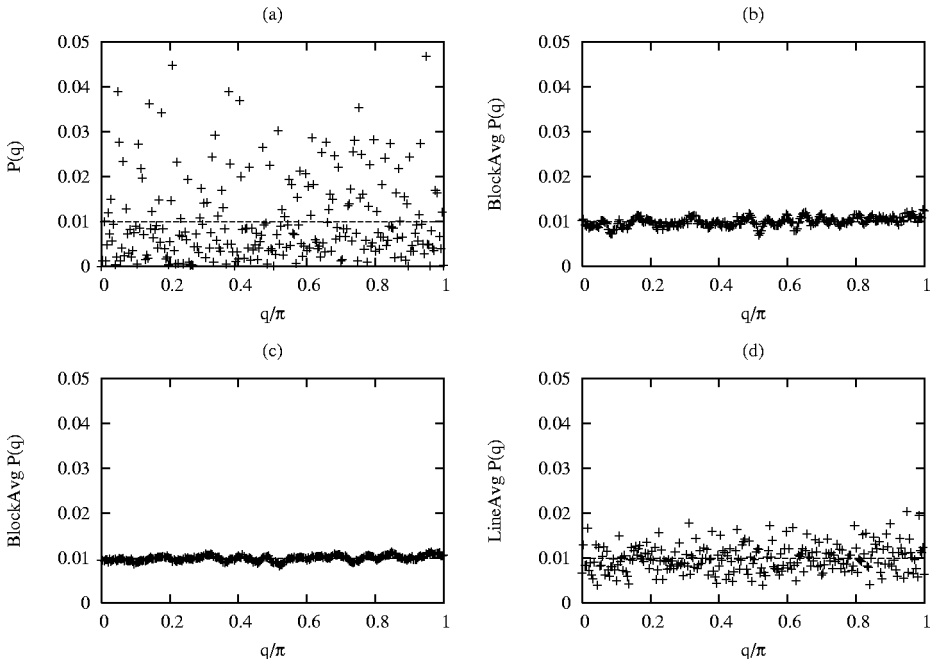

FIG. 17. Power spectrum, as defined in Eq. (A2) for a random configuration of impurities with concentration $n_i=0.01$. Here (a) shows the unaveraged results, (b) and (c) show the average over blocks of size $\Delta q_x=\Delta q_y=2\pi(2d+1)/L$ with $d=5$ and $d=10$, respectively, and (d) shows the average over lines of length $\Delta q_y=2\pi(2d+1)$ with $d=10$.

It is clear from the results shown in Fig. 17 that one can reduce the fluctuations in the power spectrum by averaging it over a region of q space surrounding a given q point. This is of course just complementary to taking the original $L\times L$ spatial lattice, breaking it up into $L_B\times L_B$ blocks with $L_B=2\pi/\Delta q$, constructing the appropriate Fourier transform for each block, and then averaging over the blocks. The more blocks one has, the smaller the rms fluctuations of the power spectrum of the Fourier transform. Of course, dividing the $L\times L$ system up into more blocks leads to a corresponding decrease in the momentum resolution. The momentum smoothing operation, Eq. (A5), is just another way of blocking.

As a further test of these ideas, we calculate the rms deviation of $\overline{P}(q)$ from n_i versus the momentum block size $2d+1$:

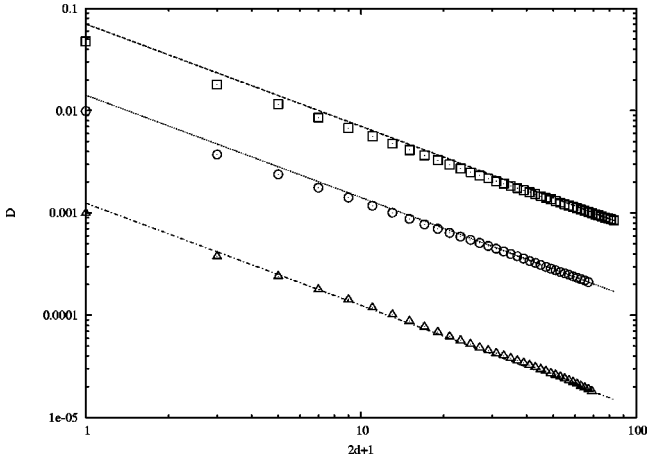

FIG. 18. rms deviation of $\overline{P}(q)$ from n_i as defined in Eq. (A6). The straight lines represent the asymptotic behavior in which $D\sim\alpha n_i/(2d+1)$.

$$D=\sqrt{\frac{1}{N}\sum_{q\neq 0}\left(\overline{P}(q)-\frac{1}{N}\sum_{q\neq 0}\overline{P}(q)\right)^2}. \tag{A6}$$

In Fig. 18 we show that D varies as $(2d+1)^{-1}$ for large d for several different concentrations of impurities. The straight lines on the plot represent the asymptotic behavior in which $D\sim\alpha n_i/(2d+1)$ with α of order one.

Finally, we model the behavior of the magnitude of the wave-vector Fourier transform of the local tunneling density of states by

$$|N(q)|=\sqrt{P(q)}\times\begin{cases}\dfrac{1}{\sqrt{q-q^\star}} & \text{if } q>q^\star=\pi/4,\\ 0 & \text{otherwise.}\end{cases} \tag{A7}$$

The results for $L=500$ and $n_i=0.01$ are shown in Figs. 19(b) and 19(c) for the BlockAvg$[|N(q_x,q_y=0)|]$, averaged over a $\Delta q_x\times\Delta q_y$ square with $d=5$ and $d=10$, respectively. Figure 19(a) shows the unaveraged result. Similarly Fig. 19(d) shows the LineAvg$[|N(q_x,q_y=0)|]$ versus q_x for the case in which we only average over a q_y segment of width $\Delta q_y=2\pi(2d+1)/L$ with $d=10$. Thus the q averaging brings out the underlying structure of the quasiparticle interference factor.

Finally, we note that even without such block averaging, one is still able to see an image of the quasiparticle interference response in an intensity plot of

$$|\overline{N}(q,\omega)|=\left|\frac{1}{\pi}\,\mathrm{Im}\,\Lambda(q,\omega)\right|\frac{|\delta\epsilon(q)|}{\sqrt{N}} \tag{A8}$$

over the (q_x,q_y) plane. In Fig. 20 we show a plot of $|\overline{N}(q,\omega)|$ for the same parameters that were used in Fig. 14. Here $|\delta\epsilon(q)|$ is obtained from Eq. (A1) with one realization of an impurity concentration $n_i=0.01$. Comparing this figure

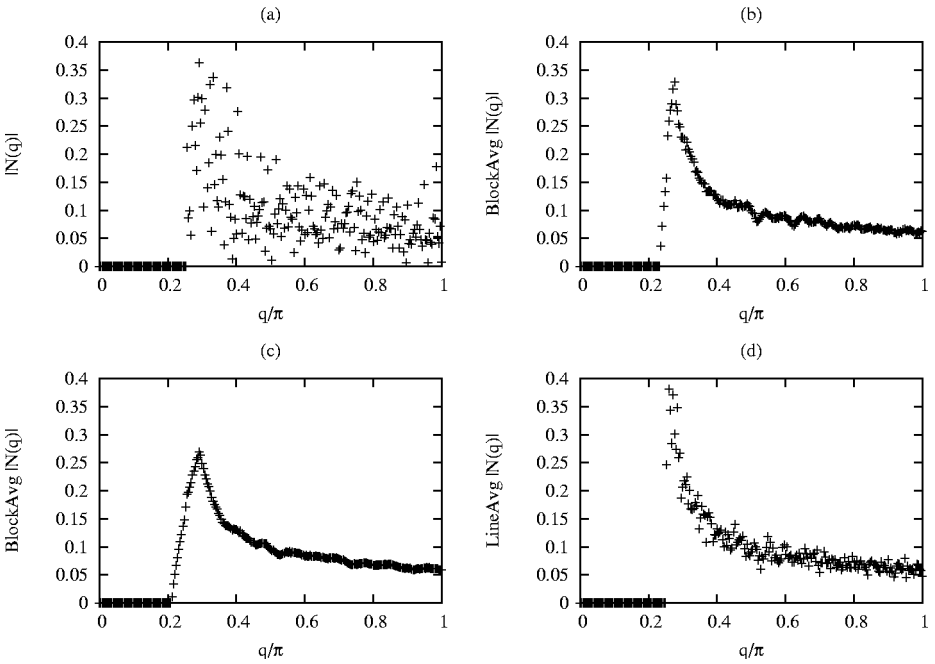

FIG. 19. The magnitude of the Fourier transform of the local tunneling density of states, as defined in Eq. (A7) for a random configuration of impurities with concentration $n_i=0.01$. Here (a) shows the unaveraged results, (b) and (c) show the average over blocks of size $\Delta q_x=\Delta q_y=2\pi(2d+1)/L$ with $d=5$ and $d=10$, respectively, and (d) shows the average over lines of length $\Delta q_y=2\pi(2d+1)$ with $d=10$.

with Fig. 14, one can see that while the structure is noisy, the key features remain clearly visible.

APPENDIX B: QUASIPARTICLE INTERFERENCE RESPONSE

The quasiparticle interference response function for the 2D free electron gas,

$$\frac{1}{\pi}\mathrm{Im}\,\Lambda(q,\omega)=\frac{1}{\pi}\mathrm{Im}\int d^2x e^{iq\cdot x}G_0(x,\omega)G_0(-x,\omega), \tag{B1}$$

can be directly evaluated using the expression for $G_0(x,\omega)$ given by Eq. (15). Since the Hankel function $H_0^{(1)}=J_0+iN_0$, we have

$$\begin{aligned}\frac{1}{\pi}\mathrm{Im}\,\Lambda(q,\omega)&=-2\pi N^2(0)\int d^2x e^{iq\cdot x}J_0(k(\omega)r)N_0(k(\omega)r)\\&=\begin{cases}8\pi N^2(0)\quad\dfrac{1}{q}\quad\dfrac{1}{\sqrt{q^2-4k^2(\omega)}}, & q>2k(\omega),\\ 0, & q<2k(\omega),\end{cases}\end{aligned} \tag{B2}$$

with $r=|x|$ and

$$k(\omega)=k_F\left(1+\frac{\omega}{\mu}\right)^{1/2}. \tag{B3}$$

We also note that carrying out the angular integration one has

$$\mathrm{Re}\,\Lambda(q,\omega)=\begin{cases}\dfrac{8\pi N(0)^2}{q^2\sqrt{q^2-4k^2}}\ln\left|\dfrac{\sqrt{q^2-4k^2}+1}{\sqrt{q^2-4k^2}-1}\right|, & q>2k(\omega),\\ \dfrac{-16\pi N(0)^2}{q^2\sqrt{4k^2-q^2}}\tan^{-}1\dfrac{q}{\sqrt{4k^2-q^2}}, & q<2k(\omega).\end{cases} \tag{B4}$$

Plots of the real and imaginary parts of $\Lambda(q\omega)$ are shown in Fig. 21. As noted, in the Born approximation one only sees $\mathrm{Im}\,\lambda(q,\omega)$. However, when the scattering is stronger, giving rise to a phase shift, both $\mathrm{Re}\,\lambda(q,\omega)$ and $\mathrm{Im}\,\lambda(q,\omega)$ will be

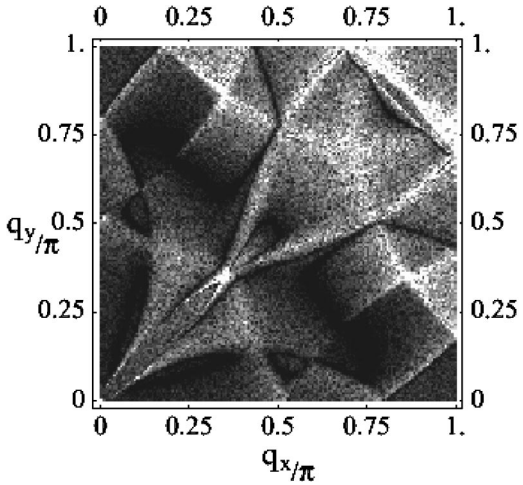

FIG. 20. Intensity map of $|\overline{N}(q,\omega)|$ for the same parameters that were used in Fig. 14. Here $|\delta\epsilon(q)|$ is obtained from Eq. (A1) with one realization of an impurity concentration $n_i=0.01$.

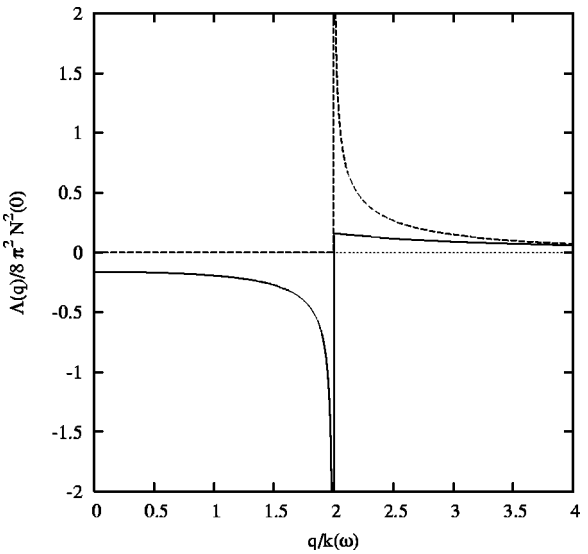

FIG. 21. The real (solid line) and imaginary (dashed line) parts of the quasiparticle interference response versus q for a noninteracting 2D electron gas.

present in the quasiparticle interference response. The imaginary part of Λ can also be evaluated by noting that, for $\omega > 0$,

$$\frac{1}{\pi}\mathrm{Im}\,\Lambda(q,\omega)=\frac{1}{\pi}\mathrm{Im}\int \frac{d^2k}{(2\pi)^2}\frac{1}{\omega-\epsilon_{k+q}+i\delta}\frac{1}{\omega-\epsilon_k+i\delta}$$

$$=2\int \frac{d^2k}{(2\pi)^2}\delta(\omega-\epsilon_k)\frac{1}{\epsilon_{k+q}-\epsilon_k}. \tag{B5}$$

Carrying out the angular integration one has

$$\int_0^{2\pi}\frac{d\phi}{2\pi}\frac{1}{\epsilon_{k+q}-\epsilon_k}=\begin{cases}\dfrac{2m}{\sqrt{q^4-4k^2q^2}}, & q^2>4k^2,\\ 0, & q^2<4k^2,\end{cases} \tag{B6}$$

so that

$$\frac{1}{\pi}\mathrm{Im}\,\Lambda(q,\omega)=2N(0)\int_{-\mu}^{q^2/8m-\mu}d\epsilon_k\,\delta(\omega-\epsilon_k)\frac{2m}{\sqrt{q^4-4k^2q^2}}, \tag{B7}$$

which gives Eq. (B2) since $N(0)=m/2\pi$.

For the electron-phonon case in which the self-energy $\Sigma(\omega)=\Sigma_1(\omega)+i\Sigma_2(\omega)$ only depends on ω, the angular integral can be evaluated in the same way, leading to

$$\frac{1}{\pi}\mathrm{Im}\,\Lambda(q,\omega)$$

$$=2N(0)\int_{-\mu}^{q^2/8m-\mu}d\epsilon_k\frac{\frac{1}{\pi}\Sigma_2(\omega)}{[\omega-\epsilon_k-\Sigma_1(\omega)]^2+\Sigma_2^2(\omega)}$$

$$\times\frac{2m}{\sqrt{q^4-4k^2q^2}}. \tag{B8}$$

Here, as usual for the electron-phonon problem we have neglected vertex corrections.

For the case of a superconductor with scattering from a site charge potential,

$$\Lambda(q,\omega)=\int \frac{d^2k}{(2\pi)^2}\frac{(\omega+\epsilon_{k+q})(\omega+\epsilon_k)-\Delta_{k+q}\Delta_k}{(\omega^2-E_k^2+i\delta)(\omega^2-E_{k+q}^2+i\delta)}, \tag{B9}$$

with $E_k=\sqrt{\epsilon_k^2+\Delta_k^2}$. For a constant s-wave gap $\Delta_k=\Delta_0$ and

$$\frac{1}{\pi}\mathrm{Im}\,\Lambda(q,\omega)=-\frac{2}{\pi}\mathrm{Im}\int \frac{d^2k}{(2\pi)^2}\frac{\omega+\epsilon_k}{\omega^2-E_k^2+i\delta}\frac{1}{\epsilon_{k+q}-\epsilon_k}. \tag{B10}$$

Making use of Eq. (B6), we have

$$\frac{1}{\pi}\mathrm{Im}\,\Lambda(q,\omega)=2N(0)\int_{-\mu}^{q^2/8m-\mu}d\epsilon_k\,\delta(\omega^2-E_k^2)$$

$$\times\frac{2m}{\sqrt{q^4-4k^2q^2}}(\omega+\epsilon_k). \tag{B11}$$

Carrying out the ϵ_k integration leads to the results given by Eqs. (36) and (37) in the text.

For a d-wave superconductor, we have

$$\frac{1}{\pi}\mathrm{Im}\,\Lambda(q,\omega)=2\int \frac{dk^2}{(2\pi)^2}\delta(\omega-E_k)\frac{1}{2E_k}$$

$$\times\frac{(\omega+\epsilon_k)(\omega+\epsilon_{k+q})-\Delta_k\Delta_{k+q}}{E_{k+q}^2-E_k^2}. \tag{B12}$$

This integral can be approximately evaluated when $\omega<\Delta_0$ for the case in which $\epsilon_k=k^2/2m-k_F^2/2m$ and $\Delta_k=\Delta_0\cos(2\theta)$. For example, for $\mathbf{q}$ along the 45° direction with $q=q_x=q_y$ and $qk_F\omega/\Delta_0$, one finds that

$$\frac{1}{\pi}\mathrm{Im}\,\Lambda(q,\omega)\simeq N^2(0)\left(\frac{1}{N(0)\Delta_0}\right)\frac{1}{k_F\sqrt{q}}\frac{1}{\sqrt{q-\dfrac{k_F\omega}{\Delta_0}}}. \tag{B13}$$

This corresponds to the contribution which comes from a momentum transfer that connects the ends of one $\omega=\sqrt{\epsilon_k^2+\Delta_k^2}$ contour [i.e., a $\mathbf{q}_7(\omega)$ wave vector] similar to the case of the ellipse discussed in Sec. III. The enhancement factor $[N(0)\Delta_0]^{-1}$ arises from the large curvature and resulting large density of states at the contours ends.

Keeping q along the 45° diagonal where $q=q_x=q_y$, there are additional square root peaks in $\mathrm{Im}\,\Lambda(q,\omega)/\pi$ which arise when $\mathbf{q}$ connects two different contours. There is a $\mathbf{q}_3(\omega)$-like peak near which

$$\frac{1}{\pi}\mathrm{Im}\,\Lambda(q,\omega)\simeq\frac{4\pi N^2(0)}{q}\left(\frac{\omega}{2\Delta_0}\right)\frac{1}{\sqrt{k_F-q}}\,\frac{1}{\sqrt{\mathbf{q}_3(\omega)-q}} \tag{B14}$$

when

$$q<q_3(\omega)=2k_F\left[1-\frac{1}{2}\left(\frac{\omega}{2\Delta_0}\right)^2\right]. \tag{B15}$$

There is also a peak associated with

$$q'(\omega)=2k_F\left(1+\frac{\omega}{\mu}\right)^{1/2}, \tag{B16}$$

where

$$\frac{1}{\pi}\mathrm{Im}\,\Lambda(q,\omega)\simeq\frac{4\pi N^2(0)}{q}\left(\frac{\omega}{2\Delta_0}\right)\frac{1}{\sqrt{q-q'(\omega)}}\,\frac{1}{\sqrt{q-q_3(\omega)}} \tag{B17}$$

when $q>q'(\omega)$. In the limit $\Delta_0\to 0$, this last expression becomes

$$\frac{1}{\pi}\mathrm{Im}\,\Lambda(q,\omega)\simeq\frac{4\pi N^2(0)}{q\sqrt{k_F}\sqrt{q-2k(\omega)}}, \tag{B18}$$

which is the free electron result Eq. (B2) for $\omega/\mu\ll 1$.

*Email address: caprio@kitp.ucsb.edu
†Email address: djs@vulcan2.physics.ucsb.edu
‡Email address: rds@physics.ucsb.edu

[1] J.M. Byers, M.E. Flatté, and D.J. Scalapino, Phys. Rev. Lett. **71**, 3363 (1993).
[2] J.E. Hoffman, K. McElroy, D.-H. Lee, K.M. Lang, H. Eisaki, S. Uchida, and J.C. Davis, Science **295**, 466 (2002).
[3] C. Howald, H. Eisaki, N. Kaneko, and A. Kapitulnik, cond-mat/0201546 (unpublished).
[4] K. McElroy, R.W. Simmonds, J.E. Hoffman, D.-H. Lee, J. Orenstein, H. Eisaki, S. Uchida, and J.C. Davis, Nature (London) (to be published).
[5] There have been various discussions of the effect of the tunneling matrix elements on the relationship between the conductance $dI(V,x)/dV$ measured on the BiO_2 layer and the local density of the states of the underlying CuO_2 layer. See, for example, I. Martin and A.V. Balatsky, Physica C **357–360**, 46 (2001). Here, for most of our present discussion, we assume that it is the local density of states $N(x,\omega)$ at the Cu site that is probed.
[6] M.E. Flatté and J.M. Byers, Solid State Phys. **52**, 137 (1999).
[7] H. Ding, J.C. Campuzano, M. Randeira, A.F. Bellman, T. Yokoya, T. Takahashi, T. Mochiku, and K. Kadowaki, Phys. Rev. B **54**, R9678 (1996).
[8] Q.-H. Wang and D.-H. Lee, cond-mat/0205118 (unpublished).
[9] A calculation of $\mathrm{Im}\,\Lambda(q,\omega)/\pi$ for the free electron case as well as a discussion of screening corrections of the scattering potential are given in S.A. Kivelson, E. Fradkin, V. Oganesyan, I.P. Bindloss, J.M. Tranquada, A. Kapitulnik, and C. Howald, cond-mat/0210683 (unpublished).
[10] We thank S. Kivelson for discussing this point with us.
[11] Here we have considered only scattering by a site charge potential; one could also consider scattering from a variation in the gap or spin degrees of freedom by changing the coherence factors in $\Lambda(q,\omega)$.
[12] W.J. Tomasch, Phys. Rev. Lett. **15**, 672 (1965).
[13] D. Podolsky, E. Demler, K. Damle, and B.I. Halperin, cond-mat/0204011 (unpublished); A. Polkovnikov, S. Sachdev, and M. Vojta, cond-mat/0208334 (unpublished).
[14] For a single-impurity configuration,

$$\frac{1}{N}\sum_q P(q)=n_i,$$

and if we drop the $q=0$ term, then

$$\frac{1}{N}\sum_{q\neq 0} P(q)=n_i(1-n_i).$$

[15] M.I. Salkola, A.V. Balatski, and D.J. Scalapino, Phys. Rev. Lett. **77**, 1841 (1996).
[16] P.J. Hirschfeld and L. Zhu (private communication).
[17] L. Zhu, W.A. Atkinson, and P.J. Hirschfeld, cond-mat/0208008 (unpublished); W.A. Atkinson, P.J. Hirschfeld, and L. Zhu, cond-mat/0301630 (unpublished).